

PPAK Integral Field Spectroscopy survey of the Orion Nebula

Data Release

S.F.Sánchez^{*1}, N.Cardiel^{1,2}, M.A.W.Verheijen³, D.Martín-Gordón⁴, J.M.Vilchez⁴, and J.Alves¹

¹ Centro Astronómico Hispano Alemán, Calar Alto, CSIC-MPG, C/Jesús Durbán Remón 2-2, E-04004 Almería, Spain.

² Departamento de Astrofísica, Facultad de Físicas, Universidad Complutense de Madrid, 28040 Madrid, Spain.

³ Kapteyn Astronomical Institute, University of Groningen, PO Box 800, 9700 AV Groningen, The Netherlands.

⁴ Instituto de Astrofísica de Andalucía, Camino Bajo de Huetor, S/N, Spain.

;

ABSTRACT

Aims. We present a low-resolution spectroscopic survey of the Orion nebula which data we release for public use. In this article, we intend to show the possible applications of this dataset analyzing some of the main properties of the nebula.

Methods. We perform an integral field spectroscopy mosaic of an area of $\sim 5' \times 6'$ centered on the Trapezium region of the nebula, including the ionization front to the south-east. The analysis of the line fluxes and line ratios of both the individual and integrated spectra allowed us to determine the main characteristics of the ionization throughout the nebula.

Results. The final dataset comprises 8182 individual spectra, which sample each one a circular area of $\sim 2.7''$ diameter. The data can be downloaded as a single row-stacked spectra fits file plus a position table or as an interpolated datacube with a final sampling of $1.5''/\text{pixel}$. The integrated spectrum across the field-of-view was used to obtain the main integrated properties of the nebula, including the electron density and temperature, the dust extinction, the $H\alpha$ integrated flux (after correcting for dust reddening), and the main diagnostic line ratios. The individual spectra were used to obtain line intensity maps of the different detected lines. These maps were used to study the distribution of the ionized hydrogen, the dust extinction, the electron density and temperature, and the helium and oxygen abundance. All of them show a considerable degree of structure as already shown in previous studies. In particular, there is a tight relation between the helium and oxygen abundances and the ionization structure that cannot be explained by case B recombination theory. Simple arguments like partial ionization and dust mixed with the emitting gas may explain these relations. However a more detailed modeling is required, for which we provide the dataset.

Key words. ISM: individual objects: M42 – (ISM:) HII regions – (ISM:) dust, extinction – ISM: abundances

1. Introduction

The Orion nebula is the brightest and best studied HII region in the sky. It has been used for decades as a fundamental laboratory in the study of the star formation regions, the ionization processes and the helium and heavy elements enrichment. However, despite the large number of studies on this target there is still a lot to know about it, even from optical studies. The more we know the more complex that it seems to be.

Several spectroscopic surveys have tried to characterize its spectroscopic properties, taken spectra at different “representative” locations (e.g., Kaler 1976, Baldwin et al. 1991, Esteban et al. 1998, Esteban et al. 2004). In particular, Osterbrock et al. (1990) and Osterbrock et al. (1992) shown a compilation of high and low dispersion deep spectra of the central bright region in the optical-NIR region (3000-11000Å). They measured 225 emission lines, 88 at the wavelength range of our IFS data. Using the relative intensities of these lines they derived the relative abundances of several elements, the electronic temperature ($T=9000$ K) and density ($N_e=4 \times 10^3 \text{ cm}^{-3}$), and the extinction ($A_V \sim 1.08$ mag, derived from the

$H\alpha/H\beta$ ratio). Such properties are frequently compared with those of distant H II regions in our Galaxy and extragalactic ones (e.g., Pagel & Isaak 1982; Ferland 2001). However, due to their distance most of these regions are poorly resolved, and their integrated properties are compared with those of particular areas in the Orion nebula.

Very little effort has been done to study the distribution of the physical properties across the nebula, apart from some peculiar areas (e.g. Baldwin et al. 1991), or their integrated values in large aperture areas. Pogge et al. (1992) performed Fabry-Perot (FP) imaging spectrophotometry on an area of $\sim 6' \times 6'$ centered in the Trapezium area. Their FP data covered the brightest emission lines in the nebula $H\beta$, [OIII] $\lambda 5007$, $H\alpha$, [NII] $\lambda 6548, 6583$, [SII] $\lambda 6716, 6731$ and HeI $\lambda 6678$. They derived some of the average spectroscopic parameters of the core of the nebula, including the integrated $H\alpha$ flux, the average extinction, the average ionization line ratios ([OIII]/ $H\beta$, [NII]/ $H\alpha$ and [SII]/ $H\alpha$), the He^+/H^+ ionic abundance ratio, and the average electron density. Evenmore, they derived the first reliable maps of the distribution of these properties across the nebula, which show a considerable degree of structure. They found significant differences with some of the previously reported values that correspond to particular regions in the nebula (e.g., Osterbrock et al. 1992). However, due to the reduced spectroscopic coverage of their dataset it was not possible to fully characterize the ionization conditions in the nebula.

Send offprint requests to: S.F.Sánchez, sanchez@caha.es

* Based on observations collected at the Centro Astronómico Hispano Alemán (CAHA) at Calar Alto, operated jointly by the Max-Planck Institut für Astronomie and the Instituto de Astrofísica de Andalucía (CSIC).

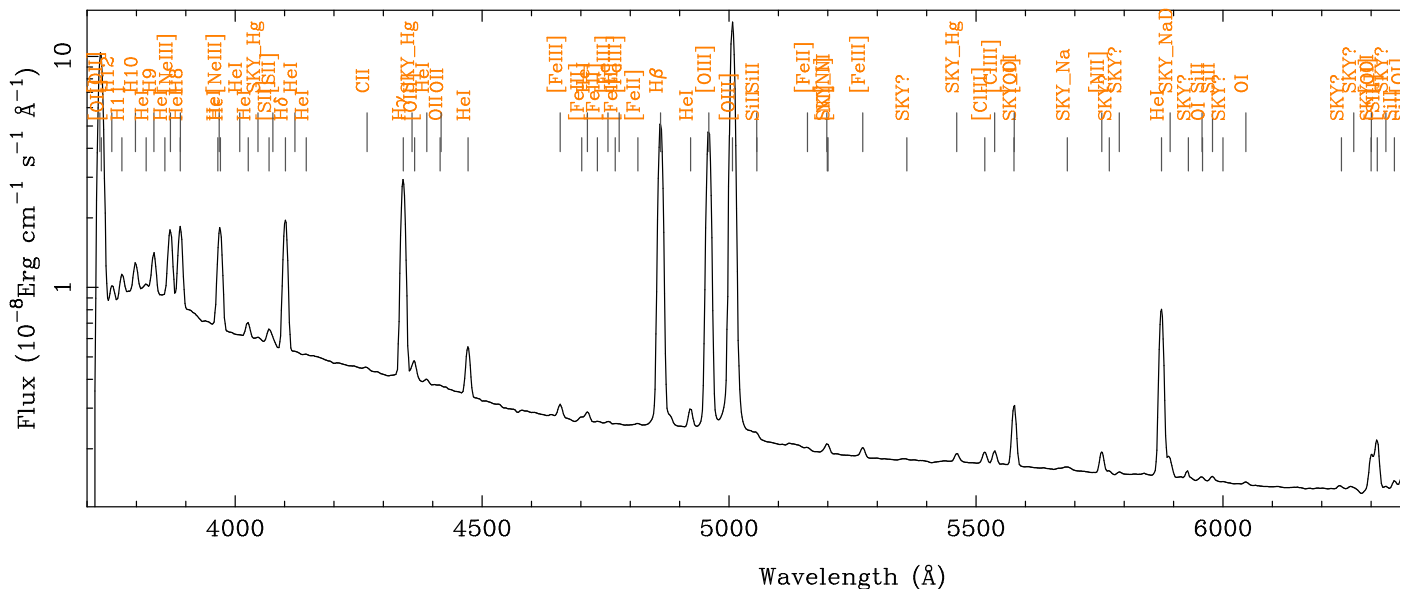


Fig. 1. Integrated spectrum of the Orion Nebula obtained coadding the 8281 individual spectra of our IFS dataset over the full field-of-view, plotted in a logarithmic scale. The identifications of the detected emission lines, as listed in Table 1, are indicated at their corresponding wavelength.

We present here a low-resolution Integral Field Spectroscopy (IFS) survey of an almost similar field-of-view of the FP observations presented by Pogge et al. (1992), but covering the entire optical wavelength range ($\sim 3700\text{--}7100\text{ \AA}$). The data have been obtained and reduced to be released publicly for the community. In this article we describe the observations and data reduction, indicating the main characteristics of the dataset, and we show a few examples of the applications of this dataset. To our knowledge this is the largest area ever sampled with an IFS unit, showing the capabilities of new techniques like 3D mosaicing to overcome the inherent reduced field-of-view of these instruments.

The layout of this article is as follow: In Section 2 it is described the observations and data reduction. Section 3 summarizes the basic properties of the dataset. In Section 4 it is listed a few examples of the applications of this dataset, including the integrated properties of the nebula, the description of the line intensity maps of some of the brightest emission lines, the distribution of the electron density and temperature, the study of the dust extinction, a description of the ionization structure, and a study of the helium and heavy elements abundances. Section 5 summarizes the conclusions of the article.

2. Observations and data reduction

Observations were carried out on November 21st, 2004 at the 3.5m telescope of the Calar Alto observatory with the Potsdam MultiAperture Spectrograph, PMAS, (Roth et al. 2005) in the PPAK mode (Verheijen et al. 2004; Kelz et al. 2006). The V300 grating was used, covering a wavelength range between 3700–7100 \AA with a resolution of $\sim 10\text{ \AA}$ FWHM, corresponding to $\sim 600\text{ km s}^{-1}$, much larger than the internal velocities within the nebula. PPAK fiber bundle consists of 382 fibers of 2.7" diameter each one (see Fig.5 in Kelz et al. 2006). Of them, 331 fibers (the science fibers) are concentrated in a single hexagonal bundle covering a field-of-view of $72''\times 64''$, with a filling factor of $\sim 65\%$. The sky is sampled by 36 additional fibers, distributed in 6 bundles of 6 fibers each one, located following a circular

distribution at $\sim 90''$ of the center and at the edges of the central hexagon. The sky-fibers are distributed among the science ones in the pseudo-slit, in order to have a good characterization of the sky. The remaining 15 fibers are used for calibration purposes, as described below.

The data were taken as a backup program of the ‘‘Disk Mass Project’’ (Verheijen et al. 2004) under bad transparency and non photometric conditions. A mosaic of 27 single exposures of 2s each one was taken. The exposure time was selected to avoid the saturation of the brightest emission lines, like $H\alpha$ and [OIII]. The initial exposure was centered in the Trapezium area of the Orion Nebula. Consecutive pointings followed an hexagonal pattern, adjusting the mosaic pointings to the shape of the PPAK science bundle. Each pointing center distances $60''$ from the previous one. Due to the shape of the PPAK bundle and by construction of the mosaic 11 spectra of each pointing, corresponding to one edge of the hexagon, overlap with the same number of spectra from the previous pointing. This pattern was selected to maximize the covered area, allowing enough overlapping to match the different exposures taken under variable atmospheric conditions. The offset procedure was carried out until closing due to risk of rain. The complete mosaic was completed in 1.5 hours in total, mostly due to the readout time of the PMAS CCD camera ($\sim 1.5\text{ min}$ in the used setup).

Data reduction was performed using R3D (Sánchez 2006), in combination with IRAF packages (Tody 1993)¹ and E3D (Sánchez 2004). The reduction consists of the standard steps for fiber-based integral-field spectroscopy. A master bias frame was created by averaging all the bias frames observed during the night and subtracted from the science frames. The location of the spectra in the CCD was determined using a continuum illuminated exposure taken before the science exposures. Each spectrum was extracted from the science frames by coadding the flux within an aperture of 5 pixels around this location along

¹ IRAF is distributed by the National Optical Astronomy Observatories, which are operated by the Association of Universities for Research in Astronomy, Inc., under cooperative agreement with the National Science Foundation.

Table 1. List of detected emission lines, uncorrected by extinction.

Wavelength Lab. (Å)	Wavelength Obs. (Å)	Flux ¹	Line Id.	Wavelength Lab. (Å)	Wavelength Obs. (Å)	Flux	Line Id.
3726.03*	3724.94	48251	[OII]	5006.84*	5006.99	140771.47	[OIII]
3728.82*	3730.08	55718.03	[OII]	5056.02	5055.80	34.23	SiII
3750.15	3751.09	921.57	H12	5056.35	5056.35	39.79	SiII
3770.63	3771.25	2131.32	H11	5158.81	5157.92	50.14	[FeII]
3797.90	3798.18	3424.23	H10	5199.00	5195.79	24.63	SKY_NI
3819.64	3819.54	1170.03	HeI3819	5197.90	5199.49	73.14	[NI]
3835.39	3835.15	4473.14	H9	5200.26	5201.02	135.71	[NI]
3857.53	3853.55	740.2	HeI	5270.40	5270.64	161.22	[FeIII]
3868.75	3868.59	10865.68	[NeIII]	5360.00	5359.94	5.64	SKY?
3888.65	3887.97	5768.53	HeI	5461.00	5461.07	198.03	SKY_HgI
3889.05	3890.22	5166.95	H8	5517.71	5517.71	260.6	[ClIII]
3964.73	3967.69	4640.82	HeI	5537.88	5537.89	256.72	[ClIII]
3967.46	3968.09	819.37	[NeIII]	5577.00	5576.40	718.87	SKY_OI
3970.07	3969.20	6984.43	HeI	5577.31	5578.10	720.08	[OI]
4009.27	4007.41	401.17	HeI	5685.00	5684.97	106.59	SKY_NaI
4026.21	4026.00	905.49	HeI	5754.64*	5754.66	359.38	[NII]
4046.00	4046.02	40.02	SKY_HgI	5770.00	5769.91	14.06	SKY?
4068.60	4068.39	567.53	[SII]	5790.00	5790.04	1.04	SKY?
4076.35	4074.88	197.45	[SII]	5875.62	5875.56	6741.14	HeI
4101.74	4101.56	14751.29	Hδ	5893.00	5892.61	311.85	SKY_NaI D
4120.86	4121.23	64.96	HeI	5930.00	5927.95	109.88	SKY?
4143.76	4148.23	27.92	HeI	5957.61	5957.11	37.47	SiII
4267.15	4265.12	100.12	CII	5958.58	5957.49	11.41	OI
4340.47	4340.32	27403.96	Hγ	5978.97	5978.80	72.62	SiII
4358.00	4364.15	129.18	SKY_HgI	6000.00	6000.26	11.52	SKY?
4363.21*	4366.73	947.65	[OIII]	6046.40	6046.57	37.43	OI
4387.93	4379.43	141.99	HeI	6240.00	6239.95	54.74	SKY?
4414.91	4471.37	2182.46	OII	6265.00	6264.91	27.57	SKY?
4416.98	4418.47	70.83	OII	6300.00	6299.33	267.31	SKY_OI
4471.50	4412.41	108.75	HeI	6300.30	6301.39	326.68	[OI]
4658.10	4658.22	412.23	[FeIII]	6312.10	6312.27	856.55	[SIII]
4701.62	4701.26	129.48	[FeIII]	6330.00	6329.99	41.77	SKY?
4713.20	4713.36	292.44	HeI	6347.09	6347.30	127.5	SiII
4733.93	4735.80	41.83	[FeIII]	6363.78	6363.72	188.39	[OI]
4754.83	4755.52	64.58	[FeIII]	6370.36	6370.53	97.66	SiII
4769.60	4775.10	64.58	[FeIII]	6548.03*	6547.63	9884.33	[NII]
4777.88	4783.04	30.95	[FeIII]	6562.82*	6562.87	158110.31	Hα
4815.55	4815.82	84.30	[FeII]	6583.41*	6583.52	30015.96	[NII]
4861.33*	4861.41	51442.9	Hβ	6678.15*	6678.37	1783.12	HeI6678
4921.93	4922.20	202.16	HeI	6716.39	6716.47*	2211.85	[SII]
4958.91*	4959.02	47031.27	[OIII]	6730.85*	6731.27	3245.46	[SII]

¹ 10⁻¹¹ Erg cm⁻² s⁻¹

* Emission line used in our analysis of the data.

the cross-dispersion axis for each pixel in the dispersion axis and stored in a row-staked-spectrum file RSS (Sánchez 2004). Wavelength calibration was performed using a He lamp exposure obtained from archive data, and corrected for distortions using ThAr exposures obtained simultaneously to the science exposures through the calibration fibers (indicated above). Differences in the fiber-to-fiber transmission throughput were corrected by comparing the wavelength-calibrated RSS science frames with the corresponding continuum illuminated ones. The nature of the dataset prevents us to perform any sky subtraction. However, due to the strength of the detected emission lines and the short exposure time, sky contamination is not an important issue for most of the foreseeable science cases.

Since the data were taken under bad weather conditions, no attempt was made to perform a flux calibration on the basis of the standard stars observed along the night. On the contrary, flux calibration was performed following a two-step procedure. First, we carried out a flux calibration using a standard star observed with a similar instrumental setup in a previous night. This pro-

cedure corrects, in first order, from the instrumental transmission. Then, we used multi-band photometric data available in the literature for the brightest star in the Trapezium, Θ^1 Ori C (Lee 1968; Vitrichenko 2000), to perform an absolute flux calibration by comparing with the un-calibrated spectrum of this object extracted from the central pointing of the mosaic. This procedure ensures a flux calibration and sky extinction correction of this central pointing.

After reducing each individual pointing we built a single RSS file for the mosaic following an iterative procedure. The spectra of each pointing was scaled to those of the previous one by the average ratio of the emission of Hβ in the overlapping spectra. To address the possible variable extinction during the observations the average ratio between these scaled spectra and the previous ones was determined. We fitted this wavelength dependent ratio to a low order polynomial function and divided all the spectra in the new pointing by the resulting wavelength dependent scale. In most of the cases this second correction has little effect on the data, indicating that the sky extinction did not

change too strongly along the observations, maybe cause they comprise only a limited amount of time (1.5h). The overlapping spectra were then replaced by the average between the previous pointing and the new rescaled spectra. The resulting spectra were included into the final RSS file, updating the corresponding position table. The process starts in the central pointing, that is flux calibrated and sky extinction corrected as explained before, ensuring an homogeneous flux calibration and sky extinction correction for all the dataset. The procedure was repeated until the last pointing was included, ending up with a final set of 8182 individual spectra and its corresponding position table. In addition to that, we created a datacube with $1.5''/\text{pixel}$ sampling by interpolating this RSS frame using E3D (Sánchez 2004).

3. Results

The final data set consists of 8182 flux calibrated spectra sampling a circular area of $\sim 2.7''$ diameter each one and covering a contiguous field-of-view of $\sim 5' \times 6'$ centered approximately in the Trapezium area of the Orion nebula. Each spectrum covers the wavelength range between $\sim 3700\text{-}7100 \text{ \AA}$, which includes the most prominent recombination and collisionally excited emission lines, from [OII] $\lambda 3727, 3729$ to [SII] $\lambda 6716, 6731$ (see Table 1). Although near the lower wavelength range, the [OII] flux was measured without problem in all fibers. The faintest detected emission lines, up to 5σ , in the individual spectra have surface brightness of the order of $10^{-14} \text{ erg s}^{-1} \text{ cm}^{-2} \text{ arcsec}^{-2}$. It is out of the scope of this article to extract all the information potentially available in this huge dataset. We are just considering here a few relevant properties of the Orion nebula using these data. Due to that, we are releasing the full dataset in order to make it freely available to the community at the project webpage².

4. Applications

4.1. Integrated properties of the Nebula

In this section we describe some of the more interesting spectroscopic properties of the nebula derived by analyzing the integrated spectrum over the full field-of-view of our IFS dataset. Contrary to previous studies that attempt to describe the average ionization conditions in the nebula by analysis individual spectra taken at different locations, we could, for the first time, describe the real average spectroscopic parameters.

4.1.1. Integrated Spectrum of the Nebula

Figure 1 shows the integrated spectrum of the Orion Nebula obtained by coadding the 8281 individual spectra of our IFS dataset, plotted in a logarithmic scale. 82 emission lines are detected in the integrated spectrum. They were identified using the list of 88 emission lines detected by Osterbrock et al. (1992) using deep spectroscopy in the same wavelength range, in combination with the list of known sky emission lines at Calar Alto (Sánchez, in prep.). The observed wavelength and integrated flux of each emission line were measured using FIT3D (Sánchez et al. 2006), removing the background continuum and deblending different emission lines when needed (and possible). Table 1 lists the detected emission lines, including, for each line, the laboratory wavelength (Osterbrock et al. 1992), the observed

wavelength, the integrated measured flux and the line identification. The final effective resolution of our integrated spectrum was $\text{FWHM} \sim 10 \text{ \AA}$, measured in the brightest detected lines. Therefore, any emission line that distances less than $\sim 3 \text{ \AA}$ from its adjacent neighbors is blended, and the listed integrated flux must be taken with care.

There is a considerable amount of blue continuum emission in the integrated spectrum shown in Fig. 1, which intensity level ranges from $\sim 10^{-8} \text{ erg cm}^{-2} \text{ s}^{-1} \text{ \AA}^{-1}$ in the ultraviolet to a few $10^{-9} \text{ erg cm}^{-2} \text{ s}^{-1} \text{ \AA}^{-1}$ in the reddest wavelength ranges. This continuum is partially due to the stars sampled by our IFS data, in particular the bright members of the Trapezium. However, it is well known (e.g., Pogge et al. 1992) that the Orion nebula presents a diffuse continuum emission, which origin is associated with the light from the stars within the ionized gas that is scattered by dust. Unfortunately, the measured continuum is strongly affected by the fact that we could not subtract the sky emission. Therefore this issue cannot be addressed properly with the current IFS data.

4.1.2. Average dust extinction

The H I Balmer series are normally used to determine the extinction. For doing so, it is required to compare the observed line ratios with the expected theoretical values. These lines are known to be emitted as a consequence of recombination, and the theory for them has been worked out in considerable detail (Hummer & Storey 1987; Osterbrock 1989). Case B (optically thick in all the Lyman lines) is the best simple approximation to describe the real physical conditions in the ionization of the gas in the Orion nebula (Osterbrock 1988; Osterbrock et al. 1992; Ferland 2001). The main deviation of the real nebula from the theory is probably the absorption of Lyman-line photons by dust mixed with the emitting gas, which observable effect are at the level of a few percent in the $\text{H}\alpha/\text{H}\beta$ ratio (Cota & Ferland 1988; Baldwin et al. 1991). Table 2 lists the observed and expected ratios between the H I Balmer series lines listed in Table 1. They show a good agreement within the errors, particularly the ratio for the 5 brightest emission lines (which errors are estimated to be lower than a $\sim 10\%$), indicating the presence of little dust extinction in average.

An average extinction of $A_V = 0.34 \text{ mag}$ is found assuming an intrinsic value of $\text{H}\alpha/\text{H}\beta = 2.86$, corresponding to case B recombination for $T = 9000 \text{ K}$ (Hummer & Storey 1987; Pogge et al. 1992; Osterbrock et al. 1992), and using the Orion extinction law of Cardelli, Clayton & Mathis (1989), with a ratio of total to selective extinction of $R_V = 5.5$ (Mathis et al. 1981). This average extinction is smaller than the value reported by Pogge et al. (1992). However, a detailed comparison of the field-of-view covered by their FP data and our IFS ones shows that their data are approximately centered $\sim 60''$ more towards the east, covering a larger area of the Orion ‘‘Dark Bay’’, an area with dust extinctions up to $A_V \sim 2 \text{ mag}$. There are better line ratios to estimate the extinction (Osterbrock et al. 1992), since, as we noted before, the intrinsic $\text{H}\alpha/\text{H}\beta$ ratio in the real nebula is a few percent smaller than the case B value (e.g. Baldwin et al. 1991). We will discuss its effect in further sections.

4.1.3. Average electron density and temperature

The electron density, N_e , in the S^+ zone of the nebula can be estimated using the observed [SII] $\lambda 6716, 6731$ doublet ratio (Osterbrock 1989). The estimated [SII] $\lambda 6716/[\text{SII}]\lambda 6731$ ra-

² <http://www.caha.es/sanchez/orion/>

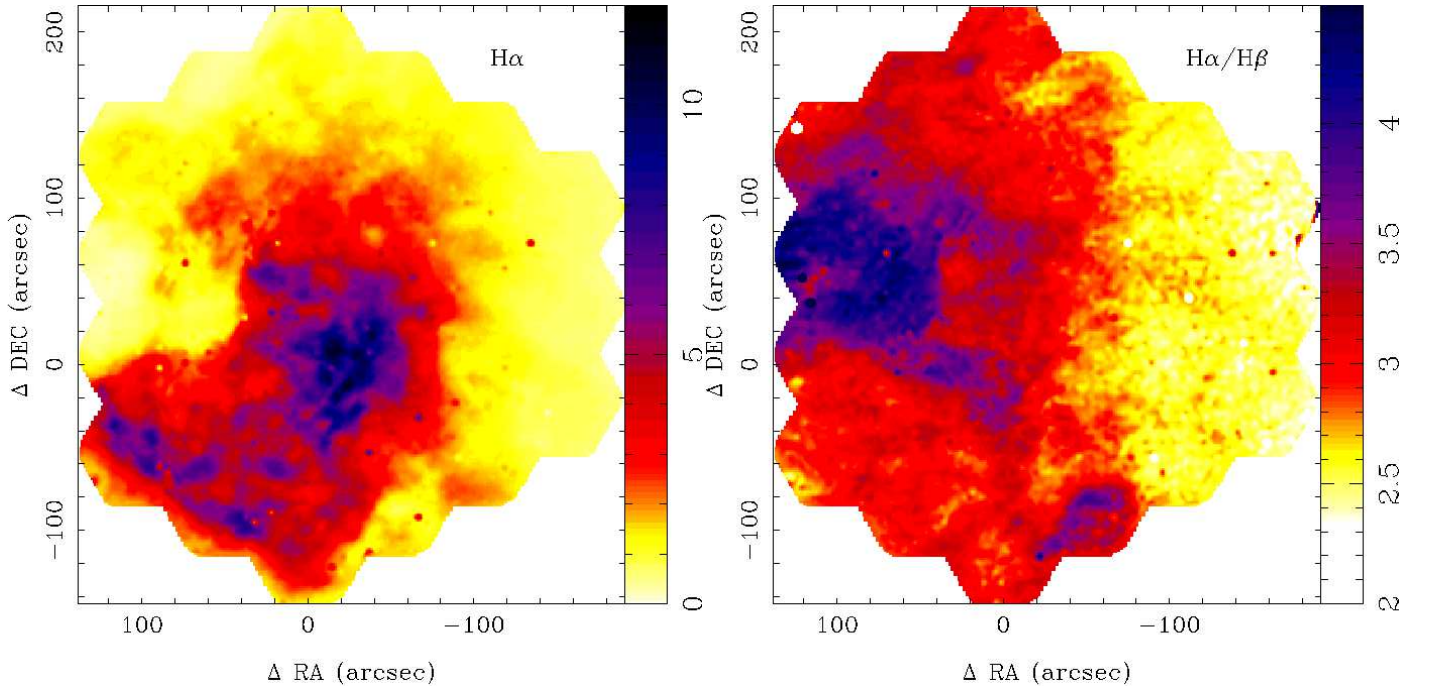


Fig. 2. Left: observed $H\alpha$ Line flux map in units of $10^{-12} \text{ erg s}^{-1} \text{ cm}^2 \text{ arcsec}^{-2}$ obtained by fitting a single Gaussian function to the $H\alpha$ emission line for each single spectrum in the dataset. The intensity map is then reconstructed by interpolating the recovered flux at the location of each spectrum, as described in the text. Right: observed $H\alpha/H\beta$ line ratio map. No correction for dust extinction was applied to any of both maps.

Table 2. Observed Balmer line ratios, uncorrected for extinction, compared with the theoretical values obtained from Osterbrock et al. 1992

Line ratio	Obs. Value	Exp. Value
$H\alpha/H\beta$	3.074	2.86
$H\gamma/H\beta$	0.532	0.486
$H\delta/H\beta$	0.287	0.259
$H\epsilon/H\beta^*$	0.136	0.159
$H8/H\beta^{**}$	0.100	0.105
$H9/H\beta$	0.128	0.0731
$H10/H\beta$	0.087	0.0530
$H11/H\beta$	0.067	0.0398
$H12/H\beta$	0.018	0.0307

* Blended with [NeIII]

** Blended with HeI

tio based on the integrated spectrum is 0.571, that can be converted to an electron density, N_e . Although mild, this conversion shows a dependency with the electronic temperature ($\sim N_e/T^{1/2}$, Osterbrock 1989). Many previous spectroscopic studies sampling the Orion nebula at different locations reported a range of temperatures between 8000-10000 K (e.g., Osterbrock et al. 1992). Therefore, the measured ratio could correspond to electron densities in a range between 2000-4000 cm^{-3} . Pogge et al. (1992) reported an average [SII] $\lambda 6716$ /[SII] $\lambda 6731$ ratio of 0.680, similar to our measurement. However, since their FP data did not cover any of the usual temperature indicators, they converted it to an electron density of $N_e = 2150 \text{ cm}^{-3}$ assuming an average temperature of 9000 K (Baldwin et al. 1991). Our IFS spectroscopic data do cover at least two of the classical indicators with enough signal-to-noise, the [OIII] ratio:

$$\frac{I(\lambda 4959) + I(\lambda 5007)}{I(\lambda 4363)} = 198.18$$

and the [NII] ratio:

$$\frac{I(\lambda 6548) + I(\lambda 6583)}{I(\lambda 7555)} = 111.02$$

Both ratios are remarkable similar to the values reported by Osterbrock et al. (1992), for the center of the Nebula, despite the evident variable conditions of the ionization across the nebula.

The conversion between both ratios and the temperature, T , depends on $N_e/T^{1/2}$ (Osterbrock 1989). Therefore, it is possible to derive the temperature using both ratios and the ratio between the [SII] doublet. Once obtained the temperature, it is possible to derive the electron density too. We found an electronic density of $N_e = 2200 \text{ cm}^{-3}$ (2056 cm^{-3}) and a temperature of $T = 10111 \text{ K}$ ($T = 8834 \text{ K}$) for the [OIII] ([NII]) ratio. To derive the electron density from the [SII] lines ratio and the temperature derived from the [OIII] lines ratios (T_3), we transformed this temperature to T_2 using the relation between both quantities presented by Pilyugin et al. (2006). Since the [OIII] $\lambda 4363$ may be affected by an unsubtracted night sky HgI emission line at $\lambda = 4358 \text{ \AA}$ we consider the estimation based on the [NII] ratio more reliable. Although the lines were not corrected by extinction, its effect on the derived temperature is negligible (even for $A_V > 2 \text{ mag}$). The average oxygen abundance, $12 + \log(\text{O}/\text{H}) \sim 8.6$, derived from the fluxes of the integrated spectrum quoted in Table 1 is close to the solar value.

Wen

4.1.4. Average ionization conditions

It is widely accepted that the ionization of the Orion nebula is dominated by photoionization by the star Θ^1

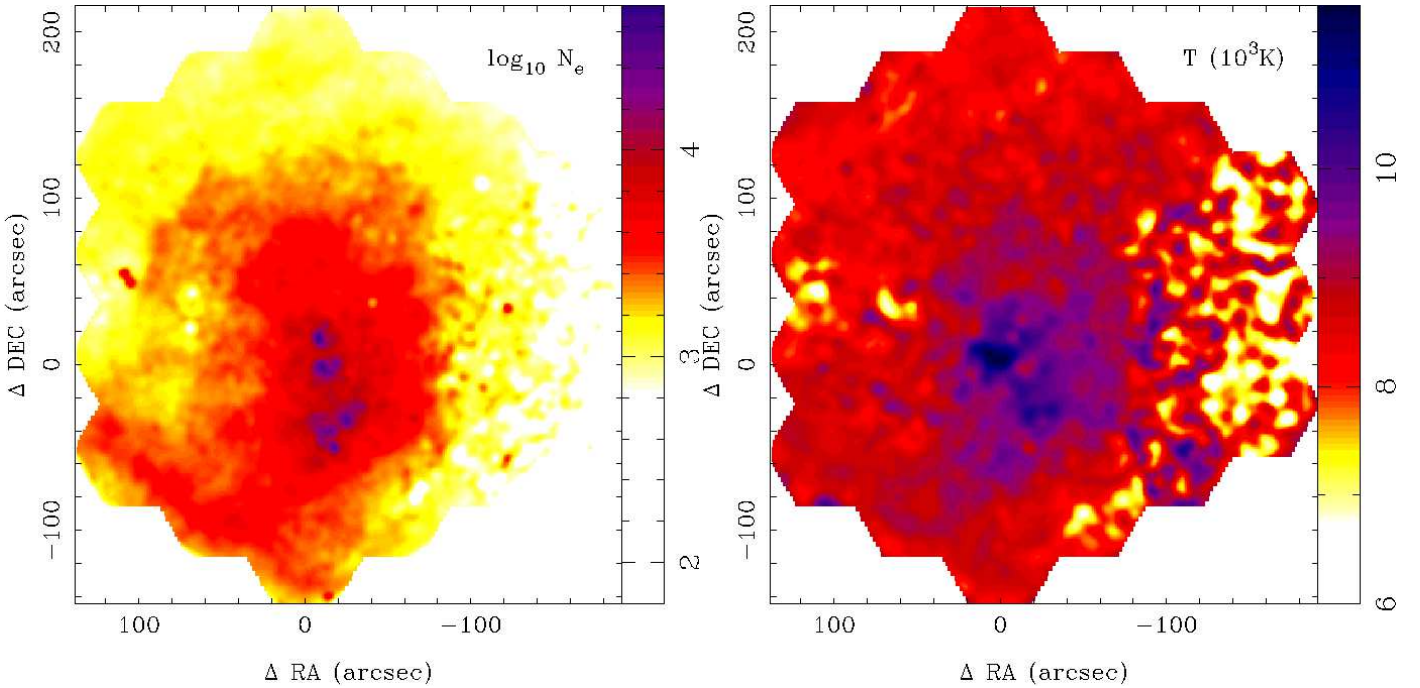


Fig. 3. Left: Electron density map, N_e in cm^{-3} , derived from the $[\text{SII}]\lambda 6716/[\text{SII}]\lambda 6731$ line ratio, represented in a logarithm scale. Right: Electron temperature map in units of 10^3K , derived from the $([\text{NII}]\lambda 6548+[\text{NII}]\lambda 6583)/[\text{NII}]\lambda 5755$ line ratio

Table 3. Integrated Spectroscopic properties of the nebula.

Parameter	Value
A_V	0.34 (mag)
N_e	2056 (cm^{-3})
T_2	8834 (K)
$[\text{OIII}]\lambda 5007/\text{H}\beta$	2.740
$[\text{NII}]\lambda 6583/\text{H}\alpha$	0.190
$[\text{SII}]\lambda 6716+31/\text{H}\alpha$	0.035

Ori C. The derived values for the classical diagnostic line ratios, $[\text{OIII}]\lambda 5007/\text{H}\beta=2.740$, $[\text{NII}]\lambda 6583/\text{H}\alpha=0.190$ and $[\text{SII}]\lambda 6716+31=0.035$, are consistent with this picture, being the typical values for H II regions ionized by OB stars (Osterbrock 1989). As already noticed by Pogge et al. (1992), the integrated $\text{H}\alpha$ luminosity, $7.6 \times 10^{37} \text{ erg s}^{-1}$ (extinction corrected), and the electron density indicate too that Orion is a rather dense, low-luminosity H II region (Kennicutt et al. 1989). Indeed, this $\text{H}\alpha$ luminosity agrees with the nebula ionization dominated by a single O 5 star (Pogge et al. 1992; Hummer & Storey 1987). A summary of the average properties of the nebula derived from our integrated spectrum is listed in Table 3.

4.2. Spatial distribution of the properties of the Nebula

While in previous sections we focused on the integrated properties of the nebula, in this section we describe the spatial distribution of these properties along the nebula. We use the 8182 individual spectra as independent probes of these properties at different locations.

4.2.1. Line Intensity Maps

The ionized gas in the Orion nebula exhibits a rather complex structure. Due to that it has been targeted by narrow-band imaging using the HST and groundbased telescopes in order to disentangle the structure of its ionized gas (e.g., Wen and O'Dell 1995; O'Dell & Yusef-Zadeh 2000, O'Dell et al. 2003, Rubin et al. 2003, and references therein). In many cases these narrow-band images catch more than one single line (e.g., $\text{H}\alpha$, the $[\text{NII}]\lambda 6548, 6583$ doublet or the $[\text{SII}]\lambda 6716, 6731$ doublet), reducing its use to study the basic parameters of the ionized gas (as listed in Table 3). As we quoted before, Pogge et al. (1992) presented FP observations that allowed to disentangle some of the main diagnostic emission lines. Following them we have obtained line emission maps for the same emission lines. In addition we have also derived line emission maps for $[\text{NII}]\lambda 5755$, $[\text{OIII}]\lambda 4363$ and $[\text{OII}]\lambda 3727, 29$, used as temperature, oxygen abundance and ionization indicators in combination with the lines quoted before. All the analyzed lines are listed in Table 1, labeled with an asterisk.

To derive the emission line maps each spectrum in the dataset was fitted to a single Gaussian function per emission line plus a low order polynomial function to describe the continuum emission using again FIT3D (Sánchez et al. 2006). Instead of fitting all the wavelength range in a row, we extracted for each spectrum shorter wavelength ranges that sampled one or a few of the analyzed emission lines, in order to characterize the continuum with the most simple polynomial function, and to simplifying the fitting procedure. In a few cases it was required to include some of these lines: e.g., $[\text{OIII}]\lambda 4363$ is blended with a night sky HgI line that must also be included in the fit. When more than one emission was fitted simultaneously, their FWHMs were forced to be equal (since the FWHM is dominated by the spectral resolution), in order to decrease the number of free parameters and increase the accuracy of the deblending process (when required). A final interpolated map with a $1''/\text{pixel}$ scale was derived for

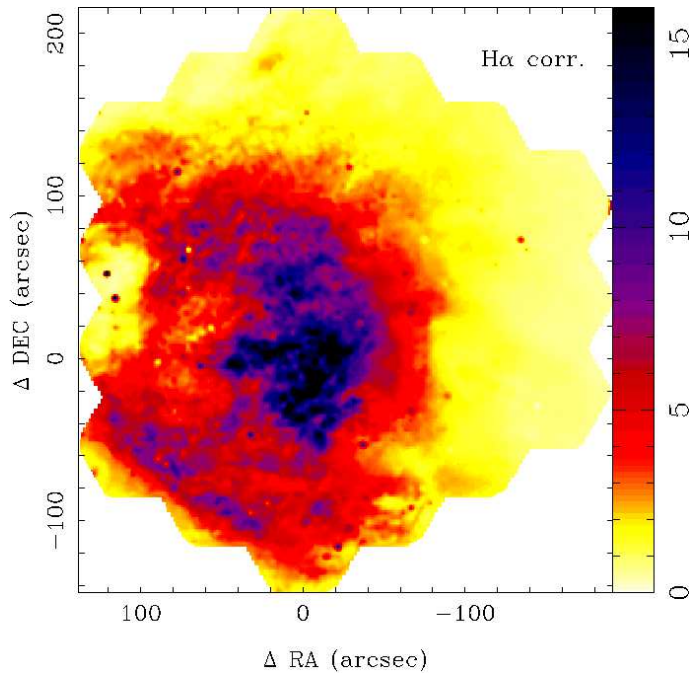


Fig. 5. $H\alpha$ intensity map corrected for dust extinction in units of $10^{-12} \text{ erg s}^{-1} \text{ cm}^2 \text{ arcsec}^{-2}$ from the uncorrected $H\alpha$ intensity map (Fig. 2), and correcting by the derived dust extinction map (Fig. 4).

each emission line by interpolating the discrete sample of intensities obtained for each spectrum (located at a certain position in the sky). The interpolation was performed using the routines included in E3D (Sánchez 2004). The data at the location of bright stars in the field were masked prior to any interpolation, in order to decrease the effects of their contamination.

Figure 2, left panel, shows the derived $H\alpha$ flux map. The well known structures of this region of the Orion nebula are easily identified: the strong $H\alpha$ emission area at the west of the Trapezium, the “Dark Bay”, a strong decrease in the $H\alpha$ intensity, at the east of the Trapezium, classically explained by dust absorption, and the Orion “Bar”, a filamentary area of strong $H\alpha$ emission at the south-east of the Trapezium. Another fainter structures, like the small arc of M42-HH2 at the north-west of the Trapezium can also be discerned. The different sub-structures seen in the reconstructed $H\alpha$ intensity map can be compared one-by-one with those in the published HST and ground-based observations, which reinforce the reliability of our adopted procedure and results. In particular, this figure can be compared with the one derived from FP observations (Fig. 1e, Pogge et al. 1992), since it does not include any contamination from [NII]. Despite the fact that there is an offset between the sampled areas of $\sim 1'$ they agree perfectly well, indicating that our final resolution must be similar to the one obtained by them (i.e., $\sim 2''$).

Figure 2, right panel, shows the observed $H\alpha/H\beta$ line ratio map. As we quoted before, this ratio can be used to trace the dust extinction when compared with the intrinsic one. The reddening of stars in the foreground of the Orion nebula is known to be small ($A_V \sim 0.2 \text{ mag}$; Breger, Gehrz & Hackwell 1981), while the reddening towards the Trapezium is much larger ($A_V \sim 1.0 - 1.4 \text{ mag}$; Osterbrock et al. 1992; Bohlin & Savage 1981). Therefore most of the extinction is associated with the nebula. Pogge et al. (1992) proposed that it must arise in the neutral gas between us and the ionized zones of the nebula. And, therefore, it is possible

to assume a simple screen geometry for the dust extinction. This assumption implies that most of the deviations of the $H\alpha/H\beta$ ratio from the expected ones are due to dust. Pogge et al. (1992) estimated an average intrinsic ratio of $H\alpha/H\beta = 2.86$ throughout the nebula, assuming case B recombination for an electronic temperature of $T = 9000 \text{ K}$ and a density of $N_e \sim 10^3 \text{ cm}^{-3}$, to derive their extinction map. Instead of using this simplification, we are able to determine both the electron density and temperature maps, and derive the expected $H\alpha/H\beta$ line ratio map for case B recombination.

4.2.2. Electron Density and Temperature

As already indicated, it is possible to determine the electron density and temperature using the [SII] $\lambda 6716, 6731$ doublet ratio and the [NII] $\lambda 6548+83$ /[NII] $\lambda 5755$ ratio. Figure 3 shows the electron density map, N_e (left panel) and the electron temperature map (right panel) derived from the indicated line ratio maps, following the formulae by Osterbrock (1989), as indicated in Section 4.1. It is important to note here that the estimated density represents only a lower limit to the real one in the hydrogen ionized zone, since the [SII] emission is also present in partially ionized regions, specially near the ionization fronts, where the density can change.

To our knowledge this is the first time that both the electron density and temperature maps are estimated simultaneously. Pogge et al. (1992) derived an electron density map using the [SII] $\lambda 6716, 6731$ doublet ratio but assumed an average temperature of $T = 9000 \text{ K}$. This approximation is basically valid, if we take into account the reduced effect of the temperature in the density estimation and the small ranges of estimated temperatures throughout the nebula (Fig. 3). This explain why, despite of the differences in the procedure to derive both maps, it is found a considerable agreement on the shape of the substructures and the covered range of electron densities between both studies ($N_e \sim 100 - 15000 \text{ cm}^{-3}$). This agreement is expected since the derivation of the electron density does not depends strongly on the temperature. However, we find a richer level of detail in the substructures in our map when compared with that of Pogge et al. (1992). Since the final spatial resolutions of both datasets are similar, we may assume that these substructures are real, most probably induced by the mild effect of the temperature in the density derivation.

The highest densities are found in two regions: (1) two clumps nearby and towards the west of the Trapezium and (2) a set of clumps at $\sim 60''$ south-southwest of the Trapezium, both regions with an electron density of the order of $N_e \sim 3 \times 10^4 \text{ cm}^{-3}$. The first region was not noticed by Pogge et al. (1992), since it was too nearby to their masked areas due to the contamination of the bright stars of the Trapezium. The second one is coincident with the observed peak in the radio continuum emission (Yusef-Zadeh 1990), and the [CII] $\lambda 158 \mu\text{m}$ IR structure detected by Stacey et al. (1992), as already noticed by Pogge et al. (1992). As we quoted above our density map is richer in substructures, and most of them are coincident with the higher resolution structures in this region. It seems that this is a dense region on the backside of the nebula (Pogge et al. 1992).

An enhance of the density occurs in the Orion bar ionization front, from $\sim 2000 \text{ cm}^{-3}$ to $\sim 4000 \text{ cm}^{-3}$, and then it drops again across the front from north-west to south-east. The regions of higher density and the detected substructures are also coincident with the areas of higher radio continuum emission in the bar (Yusef-Zadeh 1990). This is consistent with the classical picture for ionization fronts described by Hester (1991). In addition to

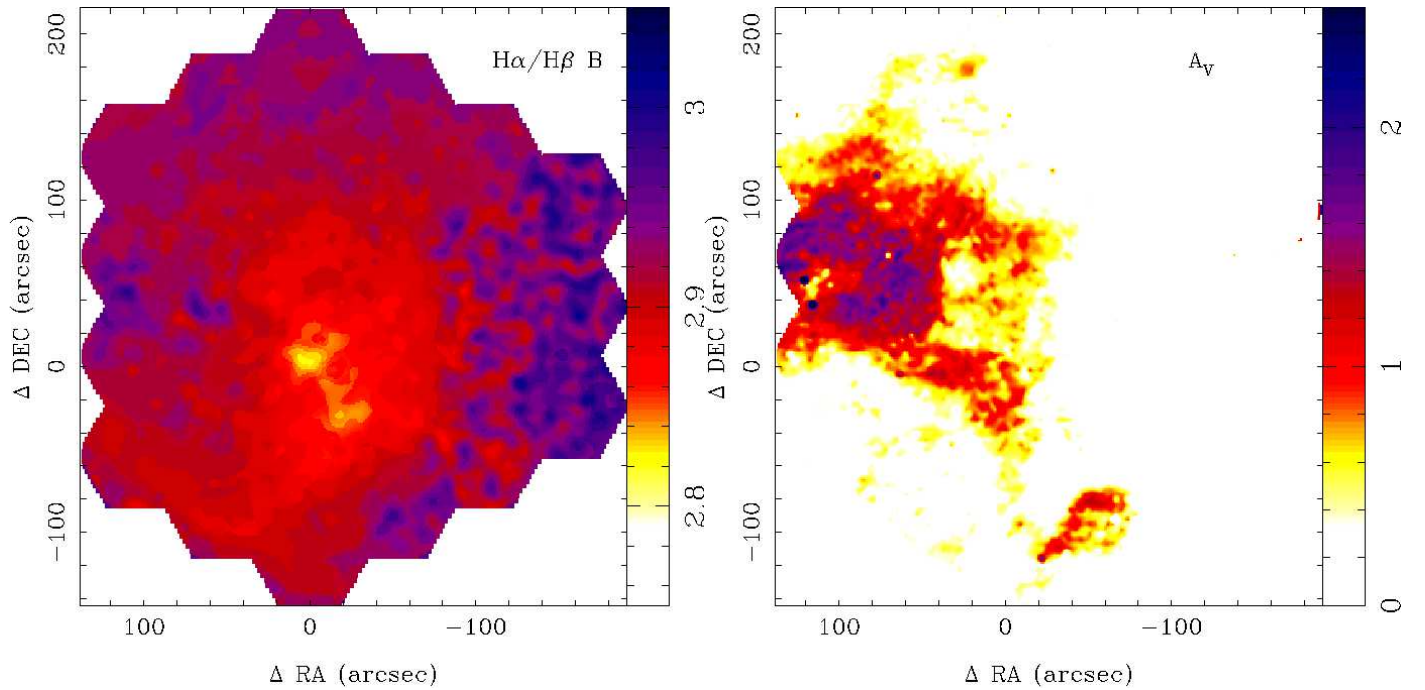


Fig. 4. Left: $H\alpha/H\beta$ line ratio map calculated for case B recombination using the electron density, N_e , and temperature maps described above (Fig.3). Right: Dust extinction map (A_V), derived comparing the measured $H\alpha/H\beta$ line ratio map with the calculated for case B recombination (left panel), and assuming the Cardelli, Clayton & Mathis (1989) extinction law.

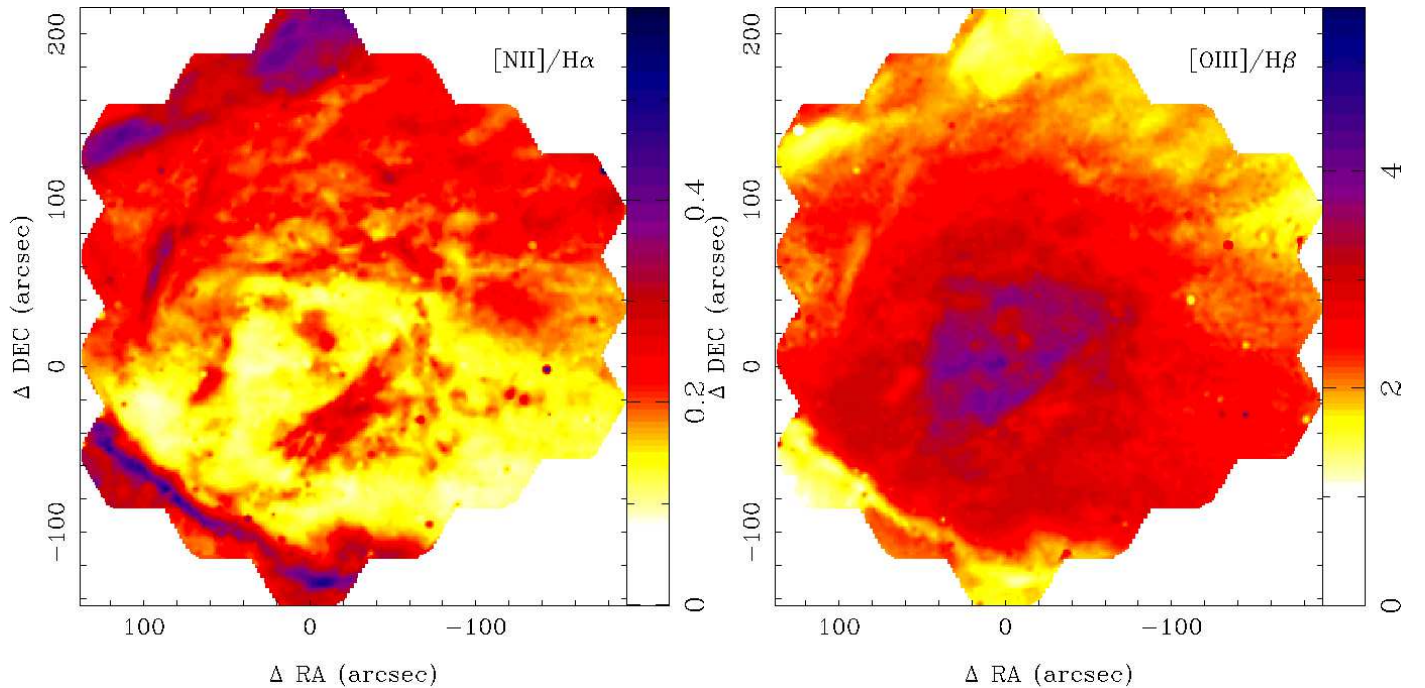


Fig. 6. Classical diagnostic line ratio maps. Left: $[NII]\lambda 6583/H\alpha$ line ratio map. Right: $[OIII]\lambda 5007/H\beta$ line ratio map.

these large structures, there are a number of isolated substructures that can be easily associated with known HH and HH-like objects in the nebula (Pogge et al. 1992), being out of the scope of the current study to describe or analyze them in detail.

As we indicated before several previous spectroscopic studies attempted to determine the ionization conditions in the Orion nebula by obtaining slit spectroscopy at different locations (e.g., Baldwin et al. 1991; Osterbrock et al. 1992; Esteban et al. 1998; Esteban et al. 2004). Most of them have determined the electron

density and temperature at these locations using the same line ratios (basically S^{++} and N^{++}) and formulae used here. Baldwin et al. (1991) obtained low-resolution optical slit spectroscopy with the slit located at $\sim 30''$ west from Θ^1 Ori C, in a east-west orientation, reaching $\sim 5'$ west. In the range covered by our IFS data they found a decay of the electron density from $\sim 6310\text{ cm}^{-3}$ to $\sim 158\text{ cm}^{-3}$ and of the electron temperature from $\sim 11000\text{ K}$ to $\sim 8000\text{ K}$. At the same location we found similar values, with the electron density dropping from $\sim 6166\text{ cm}^{-3}$ to $\sim 166\text{ cm}^{-3}$,

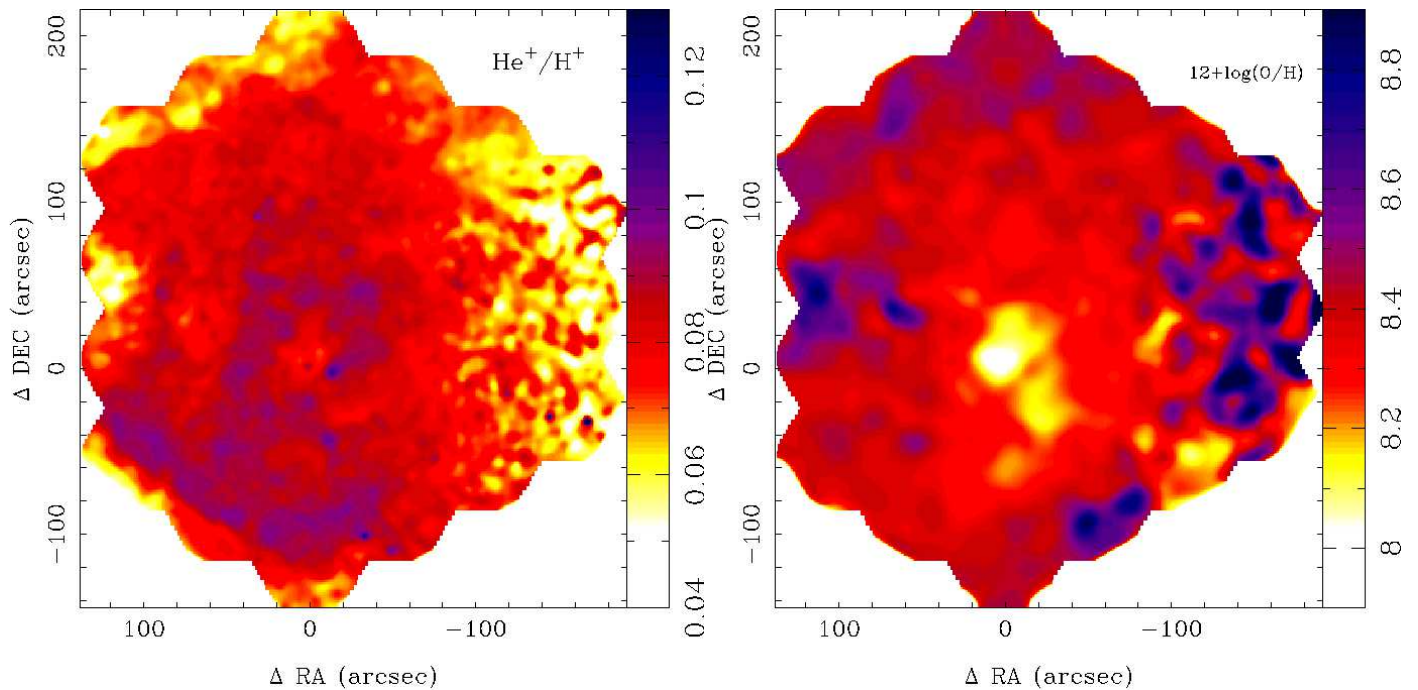


Fig. 7. Left: Map of the ionic abundance of He^+/H^+ derived from the $\text{H}\lambda 6678/\text{H}\alpha$ line ratio map corrected for the effects of extinction and collisional excitation. Right: Oxygen abundance map derived directly using the measured temperature values and intensities of the [OII] and [OIII] lines.

and the temperature from ~ 10000 K to ~ 7000 K. Esteban et al. (1998) obtained high resolution echelle spectroscopy at two locations of the nebula, one at $45''$ north and another at $20''$ south and $10''$ west of Θ^1 Ori C. New deeper data at a similar resolution were obtained by Esteban et al. (2004) in the second location. They found an electron density of 4020 cm^{-3} and 6410 cm^{-3} , and a electron temperature of 9850 K and 10710 K at each of these locations. Using our IFS data we found an electron density of $\sim 3716 \text{ cm}^{-3}$ and $\sim 7141 \text{ cm}^{-3}$ and a temperature of ~ 9743 K and ~ 10217 K at the same locations. Finally, Osterbrock et al. (1992) obtained optical and near-infrared low-resolution spectroscopy at $\sim 45''$ north of the Trapezium. They estimated the electron density and temperature to be $\sim 4000 \text{ cm}^{-3}$ and ~ 9000 K, similar to the values derived using our IFS data at a similar location.

O'Dell et al. (2003) presented a high resolution map of the electron temperature based on the [OIII] line ratio described above derived from narrow-band imaging using the WFPC at the HST. Their narrow-band images have the characteristic WFPC field-of-view of $\sim 160'' \times 160''$, located at the south-west of Θ^1 Ori C. Despite of their superb resolution, the presented image has a not much better signal-to-noise than the one derived using our IFS data. The reason for that comes from the required steps to derive the electron density from narrow-band imaging, and how they affect the signal-to-noise of the final derivation. They used a different ion to derive the electron temperature (Fig. 3). However we can compare them since there is a simple relation between both temperatures (e.g. Pilyugin et al. 2006). The values presented by O'Dell et al. (2003) in their Fig. 2 at different selected locations and the average temperature throughout all the field-of-view roughly agree with those obtained using the presented IFS data at similar locations. The temperature distribution is also coincident, however their lower signal-to-noise prevent us from a more detailed comparison. The authors claim that although they found real variations of the temperature across the

nebula, based on a statistical analysis, there is no obvious relation to the position in the nebula. Based on the temperature distribution shown in Fig. 3 we cannot agree on their interpretation of the data, since we found an obvious rich structure in the temperature distribution, which basically rises near the Trapezium and drops in the outer regions of the field-of-view of our data.

In summary, we can conclude that the electron densities and temperatures derived using the presented IFS data agree with those found using classical slit spectroscopy and narrow-band imaging at different locations of the nebula.

4.2.3. Dust extinction

Figure 4, left panel, shows the expected distribution of the $\text{H}\alpha/\text{H}\beta$ line ratio map calculated for case B recombination using the electron density, N_e , and temperature maps described above (Fig.3). We have employed the line ratios listed in Osterbrock (1989) for a discrete set of electron densities and temperatures in order to create a grid which interpolation allowed us to estimate the line ratio for any possible set of these values. This estimation is just an approximation and a more accurate one would require a complete modeling of the nebula. However, it is clearly a much better approximation than any one used in previous studies, where a single intrinsic $\text{H}\alpha/\text{H}\beta$ line ratio was estimated for the entire nebula (e.g., Osterbrock et al. 1992; Pogge et al. 1992). The estimated intrinsic line ratio ranges between ~ 2.8 and ~ 3.3 , showing a rich structure, with a clear minimum nearby the Trapezium, towards the south-east, and a second one, less prominent, at $\sim 40''$ south-west from the previous. Most of the substructures are clearly associated with fluctuations in the electron density and/or temperature (see Fig. 3).

Figure 4, right panel, shows the extinction map (A_V) derived using the observed $\text{H}\alpha/\text{H}\beta$ line ratio map presented in Fig. 2 and assuming the estimated intrinsic value of this line ratio for each position described above (Fig. 4, left panel). We used the Orion

extinction law of Cardelli, Clayton & Mathis (1989), with a ratio of total to selective extinction of $R_V = 5.5$ (Mathis et al. 1981), like in previous sections. In some locations the observed line ratio is lower than the estimated one. As we indicated previously, case B recombination is the best simple approximation to describe the physical conditions in this nebula, but it does not describe completely the ionization conditions. Indeed, the presence of dust mixed with the emitting gas decreases the real value of the $H\alpha/H\beta$ ratio by a few percent. This deviation is most probably the cause of the observed discrepancy between the estimated intrinsic line ratio and the observed one in areas with low dust extinction.

Therefore the dust extinction map shown in Fig. 4 has to be considered as a lower limit to the real one, since the intrinsic line ratio may be overestimated. The described effect is most probably not homogeneous, which prevents us from applying a single correction to the full dataset. A detailed modeling of the ionization conditions would be required to perform a better estimation on the spatial distribution of the dust extinction. Such a modeling is out of the scope of the current study, which is to demonstrate suitable applications of the presented dataset for public use. However, the approximation used is the best to the date, and any further detailed modeling would benefit of its result.

As expected the “Dark-Bay” structure is associated with an increase in the foreground dust extinction, with two extensions towards the north and the south of the Trapezium. Another peak of the extinction is located 2 arcmin south-west of Θ^1 Ori C. Similar dust extinction distributions were reported by Pogge et al. (1992) and O’Dell et al. (2000). Pogge et al. (1992) extinction map was affected by ring-like reduction artifacts, typical in Fabry-Perot data, absent in the currently presented dust extinction map. O’Dell et al. (2000) derived the extinction coefficient ($C_{H\beta}$) using two different methods: (i) by comparing high resolution radio continuum emission maps obtained with the VLA and WFPC/HST $H\beta$ narrow-band images and (ii) by deriving the $H\alpha/H\beta$ line ratio using WFPC/HST narrow-band images. In both cases it was assumed that the intrinsic $H\alpha/H\beta$ line ratio was constant across the nebula. Despite of this different approach their superb resolution extinction maps are similar to the one presented here, although the estimated values for the extinction seem to be slightly lower for the IFS data.

Figure 5 shows the extinction-corrected $H\alpha$ flux map, once the dust extinction map shown in Fig. 4 has been applied. As already noticed by Pogge et al. (1992), the appearance of the nebula is not significantly modified by the structure in the foreground dust extinction. The most remarkable structure unaffected by the dust extinction correction is the Orion bar. The decrease of the $H\alpha$ emission south-east of this structure is not due to dust extinction, but rather by a flattening of the surface of the surface of the nebula (Wen & O’Dell 1995). The “Dark Bay” is less prominent after correcting for dust extinction, but it is still present, indicating that it is not simply a region of high foreground extinction but a region with primarily absence of emission. The fact that this structure is also seen in radio continuum and CO maps (e.g., Peimbert et al. 1988; van der Werf & Goss 1989; Thronson et al. 1986), strongly supports this conclusion.

4.2.4. Ionization Structure

The ionization structure of the nebula can be in principle investigated by exploring the line ratio maps for the usual diagnostic lines (e.g., Baldwin et al. 1981; Osterbrock 1989). Figure 6 shows the line ratio maps for $[NII]/H\alpha$, left panel, and $[OIII]/H\beta$,

right panel. As already noticed by Pogge et al. (1992), the first one is the richest in structure³. The Orion bar is the most prominent substructure, clearly seen as a diagonal region south-east of the Trapezium. Another two structures are also seen as an enhance of the $[NII]/H\alpha$ ratio, one a less prominent north-south bar at the east of the Trapezium, at the edge of the “Dark Bay”, and another one at the north-east end of the field-of-view of our IFS data. The $[NII]$ emission is originated in the single ionized regions between the ionized and partially ionized zones in the nebula, tracing the rapid changes in local ionization, while $[OIII]$ is originated in the fully ionized zones (e.g., Osterbrock 1989), tracing the level of ionization in these zones. The $[NII]/H\alpha$ as well as $[OII]/H\beta$ increases in areas where the $[OIII]/H\beta$ drops, thus the maps show the effective reciprocity between both ratios.

Pogge et al. (1992) already noticed that it is not possible to use the classical diagnostic diagrams (e.g., $[OIII]/H\beta$ vs. $[NII]/H\alpha$) to distinguish between regions dominated by photoionization (HII-regions like) and regions dominated by shocks. We have repeated the experiment using our own data. They confirm that the line ratios at any position in the nebula are located in the general locus of HII-regions like objects. No major deviations are found, even in the location of well known HH objects, like M42-HH2 and M42-HH1, where shocks may play an important role. The reason is that these regions are embedded in a high surface brightness photoionization nebula. It is known that many HH objects differ in $\sim 60 \text{ km s}^{-1}$ from the systemic velocity of the nebula (e.g., Canto et al. 1980; Meaburn 1986). Thus, it is not possible to decouple them with the resolution of our dataset, requiring high spatial and spectral resolution spectroscopy.

4.2.5. He⁺ Ionic abundance and Metallicity

The Orion nebula has been used as an anchor point for HII regions to determine the primordial helium abundance (Y_p) and the slope of the relationship between the helium and heavy-element abundance enrichment (dY/dZ), (e.g. Peimbert & Torres-Peimbert 1976; Baldwin et al. 1991). However little effort has been done in order to explore possible internal effects on both quantities. Pogge et al. (1992) presented for the first time a study of the systematic behavior of the helium emission with respect to the hydrogen to understand the effects that influence the derived helium abundance. They presented the distribution of this abundance (He⁺/H⁺ map) in comparison with the ionization structure in the nebula.

Following Pogge et al. (1992) we determined the ionized helium abundance based on the HeI λ 6678/ $H\alpha$ line ratio. In ionized nebulae it is expected that the He⁺ zone is spatially included in the H⁺ one, and therefore the relative strength of HeI to HI will provide a direct estimation of the ionic abundance He⁺/H⁺ (y^+). To perform such conversion we used the effective recombination rates of Hummer & Store (1987) for HI and of Smits (1991) for HeI, recently updated by Benjamin et al. (1999,2002). Figure 7, left panel, shows the derived He⁺/H⁺ ionic abundance map, after applying a $4'' \times 4''$ median filter to increase the signal-to-noise ratio. As already noticed by Pogge et al. (1992), there is a considerable degree of structure in the Helium ionic abundance, strongly correlated with the ionization structure in the nebula. In particular, the partially ionized zones coincide with areas with lower He⁺/H⁺ abundance. In these regions, the fraction of neutral helium can be important, making necessary to correct the derive

³ The $[OIII]/H\beta$ map presented by Pogge et al. (1992) has an error of a factor 10 in the displayed scale, easily to cross-check when comparing with the values reported in their Table 2.

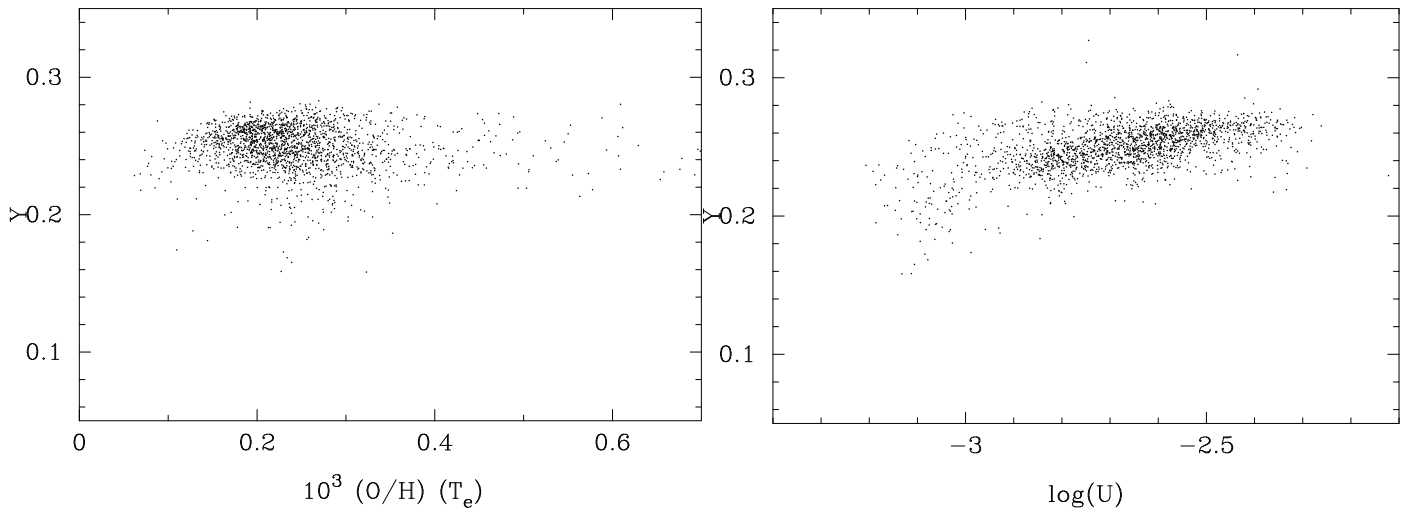


Fig. 8. Left panel: Helium mass fraction (Y) at any location of the nebula within the field-of-view of our dataset as a function of the oxygen abundance (O/H). Right panel: Helium mass fraction (Y) as a function of the ionization parameter (U).

helium abundance by this neutral fraction using an ionization correction factor (ICF).

Baldwin et al. (1992) estimated the He^+/H^+ ionic abundance at $\sim 30\text{--}90''$ west from Θ^1 Ori C in $\sim 0.0876 \pm 0.0047 \text{ cm}^{-3}$. At a similar location we estimate this value in ~ 0.089 using our IFS data. Esteban et al. (1998, 2004) estimated the electron density at the two location described before in $0.0856 \pm 0.0069 \text{ cm}^{-3}$ and $0.0893 \pm 0.0092 \text{ cm}^{-3}$. At similar locations we estimated the electron density in $\sim 0.085 \text{ cm}^{-3}$ and $\sim 0.089 \text{ cm}^{-3}$. The agreement between our results and previous studies at different locations reinforce our approach and demonstrate the quality of the presented dataset.

Figure 7, right panel, shows the oxygen abundance map using the classical direct derivation using the temperature estimator (Pagel et al. 1979). The oxygen abundance was derived using the $[\text{OII}]\lambda 3727/\text{H}\beta$ and $[\text{OIII}]\lambda 5007/\text{H}\beta$, together with the distribution of electron densities and temperatures describe before, and the formulae presented by Pilyugin & Thuan (2005). The described electron temperature, T_2 , derived using the $[\text{NII}]$ line ratio, is representative of single ionized ions (like N^+ or O^+). This temperature is slightly different than the temperature representative of double ionized ions, T_3 (like O^{++}). To derive that one it would be required to use the $[\text{OIII}]$ line ratio, as described above (Sec. 4.1). However, the strong contamination by a Hg sky emission line at $\lambda \sim 4358\text{\AA}$ to close to the $[\text{OIII}]\lambda 4363$ line prevents us to use it, particularly in the regions of faint $[\text{OIII}]$ emission. Instead we have employed the model independent relation between T_2 and T_3 presented by Pilyugin et al. (2006). For comparison purposes we also estimated the oxygen abundance ratio using the $O3N2$ indicator (Pettini & Pagel 2004), based on the $[\text{OIII}]/\text{H}\beta$ and $[\text{NII}]/\text{H}\alpha$ line ratios maps (once corrected for dust extinction). This indicator was calibrated to determine the integrated abundance in a nebula and it is not clear that it would be valid for point-to-point abundance estimations within a nebula itself. It has the advantage that it does not require the use of the poorly determined electron temperature or density, but the use of a highly signal-to-noise line ratios. Although we found a one-to-one relation between both abundances, we also found two worrisome effects: (1) there is a strong scatter in the relation, of the order of ~ 1 dex, and (2) the $O3N2$ relation induces a strong fake correlation between the oxygen abundance and any of the indicators of the degree of ionization, like the $[\text{OIII}]/\text{H}\beta$

and $[\text{NII}]/\text{H}\alpha$ line ratios and the ionization parameter (U). These two effects prevent us from using this latter indicator, although the one derived using the temperature measurement has a much lower signal-to-noise.

The derived distribution of oxygen abundance was smoothed using a $4'' \times 4''$ median filter to increase the accuracy in the areas of lower signal-to-noise. Despite of this smoothing this abundance shows also a rich structure. However, in this case there is no clear relation with the structure of the distribution of the ionization diagnostic lines, being more related to the distributions of the electron densities and temperatures shown in Fig. 3. The oxygen abundance has a minimum near the Trapezium, of the order of $12 + \log(O/H) \sim 8.2$, increasing towards the outer parts, where it reaches a level of $12 + \log(O/H) \sim 8.6\text{--}8.8$. Although in some regions its structure seems to be correlated with that of the Helium abundance, contrary to expected this is not always the case.

To test this lack of correlation the distribution of the helium mass fraction was calculated as

$$Y = \frac{4y[1 - 20(O/H)]}{1 + 4y}$$

where $y = y_o + y^+$ (Pagel et al. 1992), since y^{++} is zero given that HeII is not observed, and using the previously derived distributions of helium (y^+) and oxygen (O/H) ionic abundances. It is clear that $y^+ \rightarrow y$ when $y_o \rightarrow 0$. Therefore, in the zones with lower ionization, the fraction of y_o would be higher whereas in the areas of maximum ionization, virtually all the helium would be ionized as y^+ . Figure 8, left panel, shows this helium mass fraction as a function of the oxygen abundance, i.e., the classical figure used to derive the primordial helium abundance (Y_p) and the slope of the relationship between the helium and heavy-element abundance enrichment (dY/dZ). For doing so it is assumed a direct relation between the oxygen abundance (O/H) and that of heavy-elements (Z , e.g., $Z = 25(O/H)$, Pagel & Isaak, 1982). Only the data corresponding to regions with $\text{H}\alpha$ flux larger than $> 2 \cdot 10^{-12} \text{ erg s}^{-1} \text{ cm}^2 \text{ arcsec}^{-2}$, i.e., the areas with larger signal-to-noise, where included in this figure. There is no clear trend between both parameters, contrary to expected from the study of the integrated helium and oxygen abundances in extragalactic HII regions (e.g., Izotov & Thuan 2004). As already noticed before, there are areas of the nebula where both abun-

dances correlate, but in other ones they seem to anticorrelate. Similar deviations from the expected correlation between both parameters have been found within another nebulae (e.g., NGC 5471, Rosa 1983; Skillman 1985), showing that the ionization structure within a nebula may affect strongly this kind of relations.

It is well known that there are two ionization zones in the Orion nebula (O’de11 2001). The zone closest to the ionization front, partially ionized, where the fraction of neutral helium is not neglectible, and the zone closest to the ionizing star, fully ionized, where the fraction of neutral helium is neglectible. The former is associated with an enhance of the $[NII]/H\alpha$ ratio, while the latter is associated with an increase of the $[OIII]/H\beta$ ratio. Thus, in the partially ionized zone it would be necessary to recompute the fraction of ionized helium by applying an ICF (e.g., Vilchez 1989). To illustrate this point we estimated the distribution of the ionization parameter, U (i.e. the ratio of the ionizing photon density and the particle density), as a measurement of the degree of ionization of the nebula. We used the distribution of the $[OII]/[OIII]$ line ratio and the relation

$$\log U = -0.80 \log ([OII]/[OIII]) - 3.02$$

derived by Díaz et al. (2000). Figure 8, right panel, shows the helium mass fraction (Y) as a function of the ionization parameter (U). A similar signal-to-noise cut than in left panel was applied. Again we find a trend in the sense that highly ionized regions have higher helium abundance than less ionized regions.

The reason for such correlation and the deviations from the expected ones is not clear on the basis of case B recombination theory. However we must recall that there are at least two deviations from case B recombination in the Orion nebula: (i) there are areas in the nebula partially ionized, which may affect the estimation of the helium mass fraction in the sense that less ionized regions will show an apparently lower helium abundance, and (ii) there is evidence of an absorption of Lyman-line photons by dust mixed with the emitting gas, that affects the Balmer line ratios as we indicated above (Cota & Ferland 1988; Baldwin et al. 1991). The average oxygen abundance in the Orion nebula is similar to the solar one, as expected. However, there are regions of lower abundance, which could be explained by an oxygen depletion from the ionized gas. In this case the areas of lower oxygen abundance are also the areas with larger internal dust. If the amount of this dust correlates with the abundance of heavy elements the dust distribution may affect the correlation between the helium and heavy elements abundances. A detailed modeling is required to understand the real ionization conditions and their relation with the abundance. Such analysis is out of the scope of the current article.

Here from Fig. 8 (right panel) we can define a new methodology to derive the helium mass fraction extrapolating to U max the relation between Y versus U . In doing that we can see that the value of Y obtained for Orion is in between 0.26 and 0.28 in mass, which is the expected value fully corrected of any ICF effect. In contrast, the lowest Y values in this figure are associated to the lowest values of U , below $\log(U) \sim -3$.

5. Summary and conclusions

We have performed a low-resolution IFS survey covering all the optical wavelength range ($\sim 3700\text{--}7100\text{\AA}$) within a field-of-view of $\sim 5' \times 6'$ centered approximately in the Trapezium area of the Orion nebula. The data, comprising 8121 individual spectra sampling circular areas of $2.7''$ each one, are distributed publically as

a PPAK legacy project. To demonstrate the possible use of these data we have analysed the integrated spectrum, detecting 82 individual emission lines, which fluxes were measured. Based on these line intensities it was derived the main integrated spectroscopic properties of the ionized gas, including the average dust extinction, electron density and temperature and the values of the classical diagnostic line ratios. All of them agree with previously published results based on long-slit and fabry-perot observations.

Line intensity maps for different emission lines were obtained to study the complex structure of the ionized gas in the nebula. The derived $H\alpha$ intensity map, a tracer of the ionized hydrogen, was found to be similar to that one found using FP and narrow-band imaging, which reinforce the overall observational and reduction procedure. The electron density and temperature maps were derived using the $[SII]$ line ratios and $[OIII]$ and $[NII]$ line ratios respectively. A considerable amount of structure was found in both distributions. We used them to create a map of the expected $H\alpha/H\beta$ line ratio, based in case B recombination. A comparison between this expected line ratio and the observed one was used to obtain a dust extinction map, that was used to correct for reddening all the derived emission line maps.

The ionized structure was studied based on the classical diagnostic line ratios $[NII]/H\alpha$ and $[OIII]/H\beta$. The distribution of helium and oxygen abundances were derived based on the $HeI\lambda 6678/H\alpha$ line ratio and the temperature metallicity indicator (based on the $[OII]/H\beta$ and $[OIII]/H\beta$ line ratios). No clear relation was found between both abundance distributions, contrary to expected from the study of the integrated properties of known HII regions. There is a relation between the helium abundance and the ionization structure, in the sense that partially ionized areas are less abundant in helium and more abundant in heavy elements. Two possible deviations from case B recombination theory in the Orion nebula may explain this trend and the lack of relation between both abundances: (i) the fact that the nebula is not fully ionized, which induces to underestimate the helium mass fraction due to the non neglectible contribution of neutral helium, and (ii) the suspicion that there is dust mixed with the emitting gas which absorbs the Lyman-line ionizing photons.

A more detailed modeling is required in order to understand correctly the ionizing conditions in the nebula and their relations with the helium and heavy metals abundances. We consider that the released dataset will be of a fundamental importance to constrain such models.

Acknowledgements. We thank support from the Spanish Plan Nacional de Astronomía program AYA2005-09413-C02-02, of the Spanish Ministry of Education and Science and the Plan Andaluz de Investigación of Junta de Andalucía as research group FQM322.

MV would like to thank Matthias Steinmetz and the instrumentation group at the AIP for facilitating the construction of the PPAK module and its integration into PMAS, the spectrograph used for this survey.

We thank the referee, Prof. Dr. Prof. O’De11, who help us to improve the quality of this article with his valuable comments and suggestions.

References

- Baldwin, J. A., Phillips, M. M., & Terlevich, R. 1981, *PASP*, 93, 5
- Baldwin, J. A., Ferland, G. J., Martin, P. G., Corbin, M. R., Cota, S. A., Peterson, B. M., & Slettebak, A. 1991, *ApJ*, 374, 580
- Benjamin, R. A., Skillman, E. D., & Smits, D. P. 1999, *ApJ*, 514, 307
- Benjamin, R. A., Skillman, E. D., & Smits, D. P. 2002, *ApJ*, 569, 288
- Bohlin, R. C., & Savage, B. D. 1981, *ApJ*, 249, 109
- Breger, M., Gehrz, R. D., & Hackwell, J. A. 1981, *ApJ*, 248, 963
- Canto, J., Goudis, C., Johnson, P. G., & Meaburn, J. 1980, *A&A*, 85, 128
- Cardelli, J. A., Clayton, G. C., & Mathis, J. S. 1989, *ApJ*, 345, 245
- Clegg, R. E. S. 1987, *MNRAS*, 229, 31P

- Cota, S. A., & Ferland, G. J. 1988, ApJ, 326, 889
- Díaz, A. I., Castellanos, M., Terlevich, E., & Luisa García-Vargas, M. 2000, MNRAS, 318, 462
- Esteban, C., Peimbert, M., Torres-Peimbert, S., & Escalante, V. 1998, MNRAS, 295, 401
- Esteban, C., Peimbert, M., García-Rojas, J., Ruiz, M. T., Peimbert, A., & Rodríguez, M. 2004, MNRAS, 355, 229
- Ferland, G. 2001, PASP 113, 41
- Hester, J.J., 1991, PASP, 103, 853
- Hummer, D. G., & Storey, P. J. 1987, MNRAS, 224, 801
- Izotov, Y. I., & Thuan, T. X. 2004, ApJ, 602, 200
- Kaler, J. B. 1976, ApJS, 31, 517
- Kelz, A., Verheijen, M.A.W., Roth, M.M. et al., 2006, PASP, 118, 129
- Kennicutt, R. C., Jr., Edgar, B. K., & Hodge, P. W. 1989, ApJ, 337, 761
- Lee, T. A. 1968, ApJ, 152, 913
- Mathis, J. S., Perinotto, M., Patriarchi, P., & Schiffer, F. H., III 1981, ApJ, 249, 99
- Meaburn, J. 1986, A&A, 164, 358
- O'Dell, C. R., & Yusef-Zadeh, F. 2000, AJ, 120, 382
- O'dell, C. R. 2001, ARA&A, 39, 99
- O'Dell, C. R., Peimbert, M., & Peimbert, A. 2003, AJ, 125, 2590
- Osterbrock, D. E. 1988, PASP, 100, 412
- Osterbrock, D. E. 1989, Research supported by the University of California, John Simon Guggenheim Memorial Foundation, University of Minnesota, et al. Mill Valley, CA, University Science Books, 1989, 422 p.,
- Osterbrock, D. E., Shaw, R. A., & Veilleux, S. 1990, ApJ, 352, 561
- Osterbrock, D. E., Tran, H. D., & Veilleux, S. 1992, ApJ, 389, 305
- Pagel, B. E. J., Edmunds, M. G., Blackwell, D. E., Chun, M. S., & Smith, G. 1979, MNRAS, 189, 95
- Pagel, B. E. J., Isaak, G.R., 1982, *Philosophical Transactions of the Royal Society of London. Series A, Mathematical and Physical Sciences*, Vol. 307, No. 1487, pp. 19-35
- Pagel, B. E. J., Simonson, E. A., Terlevich, R. J., & Edmunds, M. G. 1992, MNRAS, 255, 325
- Peimbert, M., & Torres-Peimbert, S. 1976, ApJ, 203, 581
- Peimbert, M., Ukita, N., Hasegawa, T., & Jugaku, J. 1988, PASJ, 40, 581
- Pettini, M., & Pagel, B. E. J. 2004, MNRAS, 348, L59
- Pilyugin, L. S., & Thuan, T. X. 2005, ApJ, 631, 231
- Pilyugin, L. S., Vilchez, J.M., Thuan, T. X., 2006, MNRAS, 370, 1928
- Pogge, R. W., Owen, J. M., & Atwood, B. 1992, ApJ, 399, 147
- Rosa, M., 1983, in P.A., Shaver, D. Kunth, and K.Jjar (eds.), *Primordial Helium*, ESO, Garching
- Roth, M.M., Kelz, A., Fechner, T., et al., 2005, PASP, 117, 620
- Rubin, R. H., Martin, P. G., Dufour, R. J., Ferland, G. J., Blagrove, K. P. M., Liu, X.-W., Nguyen, J. F., & Baldwin, J. A. 2003, MNRAS, 340, 362
- Sánchez, S. F. 2004, AN, 325, 167
- Sánchez, S. F. 2006, AN, 327, 850
- Sánchez S.F., García-Lorenzo, B., Pecontal-Rousset, A., 2006, Proceedings of the XIII IAC Winter School, Arribas, S., Mediavilla, E., & Roth, M., Ed., in press.
- Skillman, E. D. 1985, ApJ, 290, 449
- Smits, D. P. 1991, MNRAS, 251, 316
- Stacey, G. J., Jaffe, D. T., Geis, N., Grenzel, R., Harris, A. I., Poglitsch, A., Stutzki, J., & Townes, C. H. 1993, ApJ, 404, 219
- Thronson, H. A., Jr., et al. 1986, AJ, 91, 1350
- Tody, D. 1993, "IRAF in the Nineties" in *Astronomical Data Analysis Software and Systems II*, A.S.P. Conference Ser., Vol 52, eds. R.J. Hanisch, R.J.V. Brissenden, & J. Barnes, 173.
- van der Werf, P. P., & Goss, W. M. 1989, A&A, 224, 209
- Verheijen, M. A. W., Bershady, M. A., Andersen, D. R., Swaters, R. A., Westfall, K., Kelz, A., & Roth, M. M. 2004, *Astronomische Nachrichten*, 325, 151
- Vilchez, J. M. 1989, Ap&SS, 157, 9
- Vitrichenko, E. A. 2000, *Astronomy Letters*, 26, 244
- Wen, Z., O'Dell, C.R., 1995, ApJ, 438, 784
- Yusef-Zadeh, F., 1990, ApJ, 361, L19